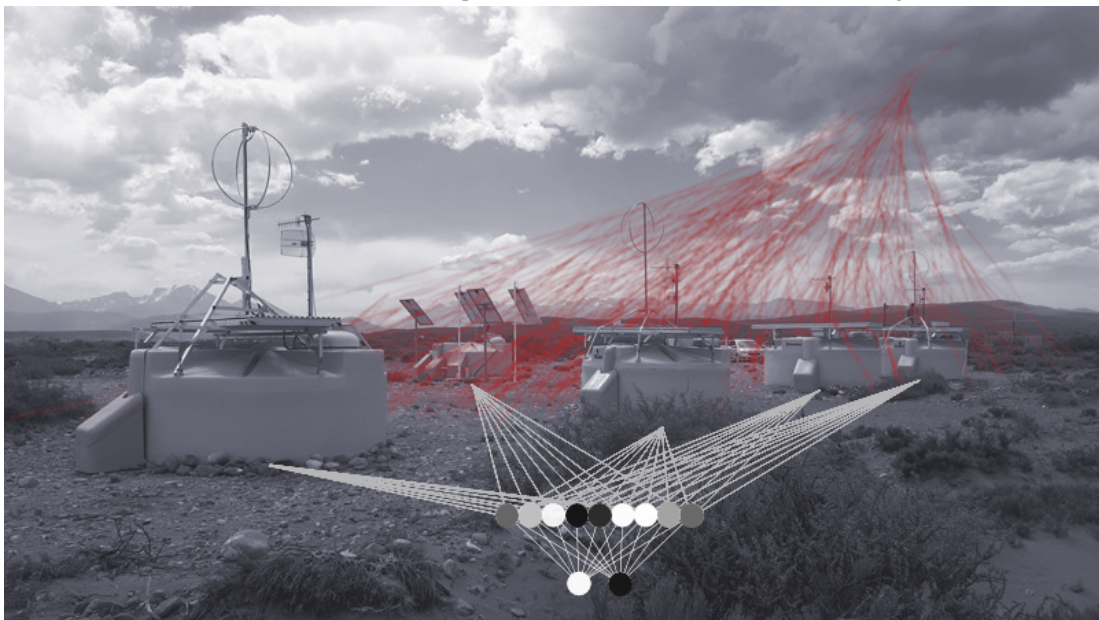# Harry Potter and the Neural network triggers for the surface detector of the Pierre Auger Observatory

Master's thesis by

Paul Filip

at the Institute for Astro Particle Physics

First Reviewer: Prof. Dr. Ralph Engel
Second Reviewer: Prof. Dr. Guido Drexlin

Processing time: 01.04.2022   –   31.03.2022

Review and Declaration

This thesis has been accepted by the first reviewer of the master thesis.

Karlsruhe, TBD

                                                                Prof. Dr. Ralph Engel

I declare that the work in this thesis was carried out in accordance with the requirements of the university's regulations and that it has not been submitted for any other academic award. Except where indicated by specific reference in the text, the work is the candidate's own work. Work done in collaboration with, or with the assistance of, others is indicated as such.

Karlsruhe, TBD

                                                                    Paul Filip

Contents

1 Physics of cosmic rays

This chapter aims to introduce the general physical principles underlaying the analysis presented in this work. For this purpose, an overview of the origin, composition and energy spectrum of cosmic rays is given in section 1.1, **??**, and section 1.3 respectively. Their interactions with other matter, the physics of extensive air showers and their possible detection methods are listed in section 1.4.

1.1 History

A first hint at the existance of high-energy particles in the upper atmosphere was given by Hess in 1912, who found that the discharge rate of an electroscope is altitude-dependant. Millikan coined the term cosmic "rays" for these particles, as he argued the ionizing radiation must be part of the electromagnetic spectrum [1]. This was later, at least partially, falsified with the discovery of the east-west effect [2]. Hess' observation however withstood the tests of time and was ultimately recognized with the Nobel prize in physics in 1936 [3]. Two years later, in 1938, Pierre Auger showed via coincidence measurements that cosmic rays in fact originate from outer space, and gave a first description of extensive air showers [4]. Another 60 years later, the Pierre Auger collaboration would adopt his experimental setup and name in their search for cosmic rays of the highest energies.

In the meantime, numerous results from different cosmic ray detectors all over the globe have helped propel the related fields of particle physics, astro physics and cosmology to new insights. Observations from cosmic ray physics serve as a valuable cross-check to the hadronic interaction models developed e.g. at CERN [5]. New theories modeling the final moments in the life of stars have arisen thanks to results from e.g. Kamiokande [6]. Last but not least publications by the Pierre Auger collaboration regarding the CR energy spectrum and flux help refine knowledge of our cosmic neighbourhood [7, 8].

1.2 Origin

Cosmic rays whose kinetic energy far exceeds their rest energy must originate from some of the most extreme environments in space. In particular, regions with large (either in field strength or spatial extent) electromagnetic fields, where charged particles can be accelerated to significant fractions of to the speed of light, via the Lorentz force.

1.2.1 Acceleration

The question of how particles gain the extremely high kinetic energies that are observed on earth is an active area of research. Since the discovery of cosmic rays, several candidate mechanisms and interactions have been identified.

Fermi Acceleration I

Super **N**ova **R**emnants (SNR) typically feature a plasma sphere propagating outwards from the former stars core into the **I**nter**S**tellar **M**edium (ISM), in this region of plasma any magnetic field lines will be comoving, according to Alfvén's theorem [9]. First realised by its' namesake Fermi, such SNR shock fronts serve as source of high-energy CRs [10].

If a low-energy particle is injected into the SNR shock front, it will eventually be reflected by the local $\vec{B}$-field, analogous to a magnetic mirror, or elastic collision. If $\frac{\mathrm{d}\mathbf{B}}{\mathrm{d}t} = 0$, this does not cause the particle to gain any energy, espically because $W = \vec{F}_{\mathrm{L}} \cdot \vec{r} \propto (\vec{v} \times \vec{B}) \cdot \vec{r} = 0$. However, because the $\vec{B}$-field is moving radially outward, a net energy of

$$\Delta E = \beta_{\mathrm{SNR}} \cdot E_0 \tag{1.1}$$

arises, where $\beta_{\mathrm{SNR}} = v_{\mathrm{SNR}} / c$ and E_0 are the velocity of the shock-front and the initial energy of the particle. From chapter 7 in [10] it follows that ionization losses within the shock front are not completely negligible. Hence a particle must have a sufficient energy to have a net positive change according to Equation 1.1. This is the injection energy, and of the order of 200 MeV for protons. Also, because typically $\beta_{\mathrm{SNR}} \leq 0.10$ a single acceleration cycle is not enough to explain the CR energies observed on earth. Instead, multiple cycles are needed. This requires the need for additional, focusing $\vec{B}$-fields, provided for example by the ISM, which alter the trajectory of injected particles such that they can be reflected off the shock-front again.

With each cycle, the particles rigidity $R = |\vec{p}|c / q$ increases, until its gyroradius $\rho = R/|\vec{B}|$ exceeds the spatial extent of the focusing $\vec{B}$-field and the particle escapes into space. With an effective ejection probability p per cycle, the energy after n cycles and the expected energy spectrum, $\Phi(E)$, becomes

$$E(n) = E_0 \ (1 + \beta_{\mathrm{SNR}})^n . \tag{1.2}$$

$$N(n) = N_0 \ (1-p)^n$$

$$\Leftrightarrow \quad \log\left(\frac{N(n)}{N_0}\right) = n \cdot \log\left(1-p\right)$$

$$\Leftrightarrow \qquad\qquad = \log\left(\frac{E(n)}{E_0}\right) \frac{\log 1 - p}{\log 1 + \beta_{\mathrm{SNR}}}$$

$$\Leftrightarrow \qquad N(E) = N_0 \cdot \left(\frac{E(n)}{E_0}\right)^{\log(1-p) \ / \ \log(1+\beta_{\mathrm{SNR}})}$$

$$\Rightarrow \qquad \Phi(E) = \frac{\mathrm{d}N}{\mathrm{d}E} \propto E(n)^{\alpha-1}, \tag{1.3}$$

where $\alpha = \frac{\log(1-p)}{\log(1+\beta_{\mathrm{SNR}})}$ in Equation 1.3 is a spectral coefficient whose exact value will depend on the age of the SNR (β_{SNR} decreases with age), the injected particle (different primaries have different injection energies and ejection probabilities), as well as many other factors that are often not known a priori. In any case, it can be observed that the expected spectrum is a power law in the ranges from injection energy to maximum energy, which arises due to the finite lifetime of the SNR.

Fermi Acceleration II

1.2.2 Composition

1.3 Energy spectrum

1.4 Extensive air showers

2 The Pierre Auger Observatory

Located on the argentinian high-plains of Pampa Amarilla, the Pierre Auger observatory is a hybrid detector designed to detect and study cosmic rays of the highest energies. With an effective area of $3000\,\text{km}^2$ it is by far the largest experiment of its kind [11].

Altough first proposed in 1992, it took 18 years until the idea of a large scale experiment to detect cosmic rays matured and construction of the first prototype started near Mendoza [12]. Some further 20 years later, the Pierre Auger collaboration has co-authored over publications and continues to advance research in astroparticle physics.

It does this via a hybrid approach, combining measurements of a **S**urface **D**etector (SD) as well as a **F**louresence **D**etector (FD). Additional machinery, such as the e**X**treme (XLF) and **C**entral **L**aser **F**acility (CLF), is installed to monitor atmospheric variables. This improves the overall systematic accuracy of predictions made by the experiment. An overview of the site can be seen in Figure 2.1. Data measured by the FD, SD and the atmospheric monitors is sent to a **C**entral **D**ata **A**cquisition **S**ystem (CDAS) located in the nearby town of Malargüe.

This chapter offers a brief look into the measurement principle and setup of the observatory. Information regarding the fluoresence detector can be found in section 2.1. The SD is described in section 2.2. A more in depth read on detector specifications and design choices is represented by the Pierre Auger observatory design report [11], where a lot of information stated in this chapter is conglomerated from. Notes on the event reconstruction are listed in section 2.3 and summarized from [13] and [14].

2.1 Fluoresence Detector (FD)

The FD consists of a total of 27 fluoresence telescopes (eyes) at 4 different sites. Each eye monitors a $30° \times 30°$ window of the sky at a resolution of $\approx 0.5\,\frac{\text{px}}{\text{deg}^2}$. This results in an effective FOV of roughly $180° \times 30°$ per FD station, with an exception of Coihueco, where three additional telescopes - HEAT (**H**igh **E**levation **A**uger **T**elescope) - are installed to enable monitoring of higher zenith angles ($30° \leq \theta \leq 60°$) and increase sensitivity for showers of lower energies (compare chapter 1). A schematic of the setup of each eye is given in Figure 2.2a.

The individual telescopes consist of $3.6\,\text{m}$ by $3.6\,\text{m}$, convex mirrors. They reflect incoming light onto a set of 440 photomultipliers (PMTs), each corresponding to one pixel in the resulting image seen by an eye. Since the setup needs to be extremely sensitive to UV light in order to detect flouresence caused by extensive air showers, its operation is limited to the relatively noise free moonless astronomical nights (Sun
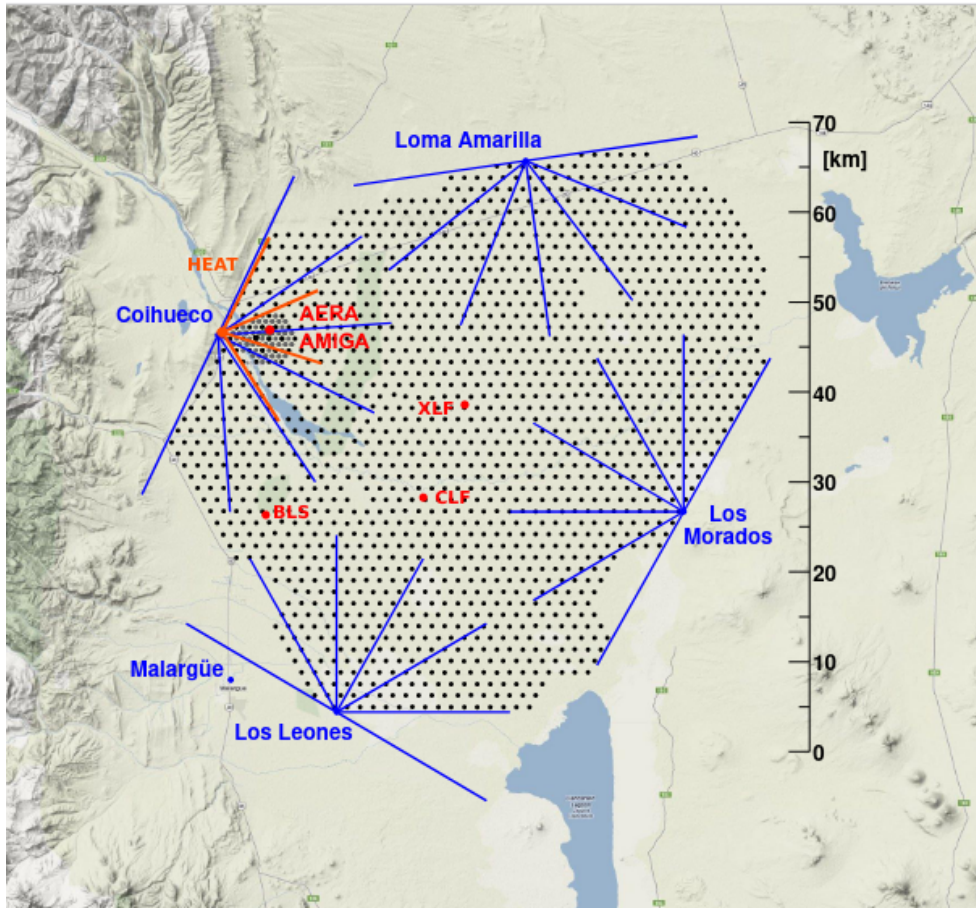
Figure 2.1: Overview of the Pierre Auger observatory. The four different FD sites (respective FOV shown with blue lines) sit at the edge of the detector area and monitor the night sky above the SD array consisting of 1600 water tanks (black dots). A denser spacing of stations near Coihueco is equipped with additional electronics such as e.g. radio antennas (AERA) and muon detectors (AMIGA). Image taken from [15]
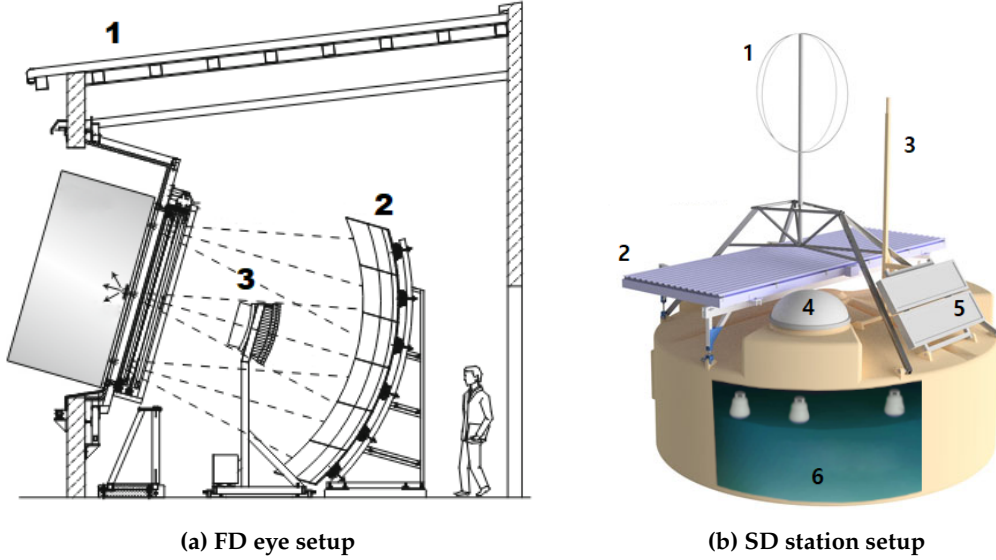
.

(a) FD eye setup   **(b) SD station setup**

Figure 2.2: (a) Schematic view of an FD eye with housing (1), main mirror (2) and camera (3). Image taken from [14] **(b)** Setup of an SD WCD with radio antenna (1), SSD (2), communication and GPS antenna (3), electronics box (4), solar panesl (5) and the WCD (6). Image adopted with changes from [16] and [17]

$\angle$ Horizon $\lesssim -18°$). When the FD is operational, this allows the observation of the longitudinal propagation of a shower instead of just its' footprint (as seen by the SD).

2.2 Surface Detector (SD)

The SD consists of 1600 individually operating stations, spaced apart on a hexagonal grid with a standard 1.5 km spacing. Each station is made up of a main tank filled with 12 000 L of purified water and reflective inner walls, a solar panel and batteries for power management, as well as an antenna for communication. Within each tank three PMTs detect Cherenkov light originating from shower particles, these are together with the tank referred to as **W**ater **C**herenkov **D**etectors (WCDs). With the (at the time of this work) ongoing AugerPrime upgrade, each station is additionally equipped with a **s**mall **PMT** (sPMT), **S**urface **S**cintillator **D**etector (SSD), and radio antenna atop the tank. This allows for the recording of stronger signals, finer separation of electromagnetic and muonic shower component and detection of highly inclined air showers respectively [18, 19]. Figure 2.2b shows a schematic blueprint of each SD station.

2.2.1 Data acquisition (DAQ)

Onboard electronics, the **U**pgraded **U**nified **B**oard (UUB), or more precisely six 10-bit **F**lash **A**nalog-to-**D**igital-**C**onverters (FADCs) read out measurement data from the PMTs at a sampling rate of 120 MHz (≈ 8.33 ns binning) [20]. This is done in a two-fold

way. Three FADCs digitize the PMTs dynode voltage, resulting in the **H**igh **G**ain (HG) output. Three FADCs monitor the anode voltage to form the **L**ow **G**ain (LG) output, which can be analyzed if the HG output exceeds a value of 2^{10} ADC counts and becomes saturated. This effectively enables the measurement of both large ($\geq O(10^3)$ particles hitting the tank) as well as small shower signals ($O(1)$ particle hitting the tank) with sufficient accuracy [13]. Once an FADC bin has been recorded and checked for possible triggers (c.f. **??**) it is written to a ring buffer. If a trigger is issued, the corresponding chunk in the ring buffer ($\approx 4.992\,\mu s$ (599 bins) before and $12.07\,\mu s$ (1448 bins) after a trigger, $2047 + 1$ bins total), the measured trace, can be analyzed in order to calibrate a station in the array (subsection 2.2.3, subsection 2.2.2) or processed by a higher-level CPU for event reconstruction purposes (see section 2.3).

While each station is equipped with the same electronics and runs the same analysis software, variables like the position in the field, station age or slight changes in the manufacturing/installation process cause different stations to age differently. Over the lifetime of the array such differences can sum into potentially drastic discrepancies in gathered data. Put simply, an extensive air shower will look different both to different WCDs at the same time as well as the same WCD at different times. To account for this, measurements are standardized across all stations. ADC counts are related to a **V**ertical **E**quivalent of through-going **M**uons (VEM) that would result in the same signal strength. In this fashion, the maximum response that is generated by a PMT from one vertically through-going muon is defined as $1\,\text{VEM}_{\text{Peak}}$. The total deposited charge (equivalent to the integral of the response) is defined as $1\,\text{VEM}_{\text{Ch.}}$. The conversion factor between ADC counts and VEM_{Peak} and $\text{VEM}_{\text{Ch.}}$ (referred to as I_{Peak} and Q_{Peak} respectively) is estimated from data and continuously updated separately for each station. Note that due to the limited computational resources of the WCD, as well as constraints on the amount of data that can be transmitted per station in the SD array ($1200\,\frac{\text{bit}}{\text{s}}$, [21]), a simplified, rate-based approach is implemented for autonomous calibration in the field (Online calibration), this stands in contrast to the more physics-driven histogram method used during event reconstruction (Offline calibration). In any case, both algorithms are listed in the following subsections and discussed in more detail in the referenced literature.

2.2.2 Offline calibration

Baseline estimation

In order to estimate I_{Peak} and Q_{Peak} of a WCD tank first the baseline - the average response in the absence of any signals - of each PMT needs to be determined. All further analysis will then be based on the baseline-subtracted PMT data.

For event reconstruction, a first baseline estimate of a WCD PMT is predicted by examining the beginning and end of a 2048 bin ($17.06\,\mu s$) long trace. The mode m as well as standard deviation σ of the first (last) 300 bins is calculated. All bins larger or smaller than $m \pm 2\sigma$ are truncated and removed from the trace window. The value of m, σ is consequently updated and the procedure repeated until a convergence is

reached and no further cut is necessary. The best estimate B_{front} (B_{end}) for the front (end) of the trace at this point is given by the mean value of all remaining bins. It's statistic uncertainty $\sigma_{B_{\text{front}}}$ ($\sigma_{B_{\text{end}}}$) is given by the standard deviation of the remaining bins [22]. The baseline between the flat front and end estimate is then interpolated based on the difference

$$\Delta B = B_{\text{end}} - B_{\text{front}}. \tag{2.1}$$

- **Rejection of anomalous upward fluctuations $\frac{\Delta \mathbf{B}}{\sigma_{\Delta \mathbf{B}}} \geq +10$:**

  B_{end} being higher than B_{front} often indicates errors in the electronic readout or defect components in the measurement chain. There exists no physical reason why the end baseline should be (significantly) higher than the front. Consequently, traces where this is the case are ignored during event reconstruction.

- **Constant approximation for small upward fluctuations $+5 > \frac{\Delta \mathbf{B}}{\sigma_{\Delta \mathbf{B}}} \geq 0$:**

  Small fluctuations of the baseline are expected and the norm. If these fluctuations are positive ($B_{\text{end}} > B_{\text{front}}$) the method of calculating the mode, truncating outliers and repeating both steps is applied to the entire length of the signal, resulting in a constant baseline estimate B across the trace.

- **Step-function approximation for small downward fluctuations $0 > \frac{\Delta \mathbf{B}}{\sigma_{\Delta \mathbf{B}}} \geq -1$:**

  Unlike positive fluctuations, negative fluctuations ($B_{\text{end}} < B_{\text{front}}$) can have a physical significance. Due to the undershoof of PMTs after detecting a signal in the WCD (compare [**glietta2008recovery**]), the baseline estimate decreasing towards the end of the trace often indicates the presence of shower particles within the tank. For this reason, downward fluctuations are handled differently from upward ones. If the fluctuations are sufficiently small, the baseline across the trace is estimated as a simple step-function; The trace is separated into two parts along its' maximum ADC value. The front part (i.e. before the max. value) has the baseline B_{front}, while the rear part is estimated by B_{end}. An example of this is shown in Figure 2.3a.

- **Charge-linear approximation for large undershoots $-1 \geq \frac{\Delta \mathbf{B}}{\sigma_{\Delta \mathbf{B}}}$:**

  For larger undershoots, the baseline is estimated bin by bin based on the deposited charge in the detector. Starting with a value of B_{front} for the bins 1-300, the remaining baseline is first linearly interpolated according to Equation 2.2,

$$b_i = B_{\text{front}} - \Delta B \cdot \frac{i - 300}{1448}, \qquad 300 \geq i \geq 2048, \tag{2.2}$$

where the magic numbers 300 and 1448 refer to the last bin of the front baseline estimate and the length of the interpolated baseline respectively. From this, the deposited charge q_i up to bin i can be calculated as per Equation 2.3.
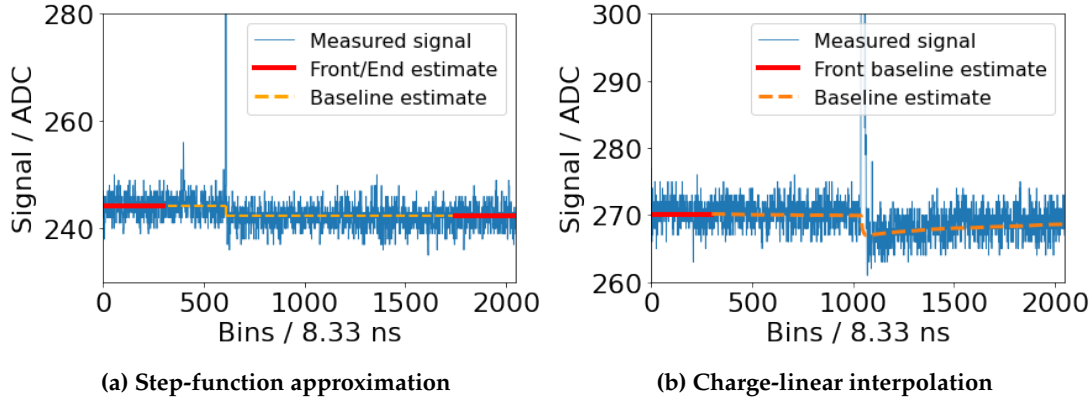
(a) Step-function approximation

(b) Charge-linear interpolation

Figure 2.3: (a) A simple step function is sufficient to accurately model a PMTs' noise level at small downward fluctuations. **(b)** For larger discrepancies the more involved charge-linear interpolation is used. Note that the signal undershoot is exaggerated for visualization purposes in both examples.

$$q_i = \sum_{k=0}^{i} (T_k - b_k) \exp\left(-\frac{8.33\,\text{ns}}{\tau} \cdot (i - k)\right) \tag{2.3}$$

In Equation 2.3, T_k refers to the numerical value of bin k. Note that an exponential falloff term has to be added to account for the decay in signal undershoot with a decay time of $\tau = 45\,\mu\text{s}$. The value of τ is determined in [23]. Assuming the magnitude of the signal undershoot is directly proportional to the deposited charge q, a correction of the baseline thus becomes

$$b_i = B_{\text{front}} + \frac{q_i}{q_{1898}} \cdot \Delta B. \tag{2.4}$$

The parametrization in Equation 2.4 is chosen such that the charge-interpolated baseline at bin 1898 (the center position in the last 300 bins) is exactly equal to the rear baseline estimate B_{end}. The prediction can be made more accurate by repeating the above steps, each time recalculating q_i and readjusting the baseline b_i in the process. Figure 2.3b shows an example baseline estimate after three such iterations. In general, it converges to a robust estimate within five repetitions [23].

Estimation of I_{Peak} and Q_{Peak}

The conversion factor between ADC counts and VEM$_{\text{Peak}}$, VEM$_{\text{Ch.}}$ are built from distributions of traces that satisfy the muon trigger, which scans incoming ADC bins for a value exceeding the muon threshold $t_\mu = b + 30\,\text{ADC}$, 30 ADC above baseline, for any of the three WCD PMTs. If this requirement is met, 69 bins (19 before, trigger bin, 49 after) are written to the muon buffer, a FIFO (first-in-first-out) type memory storage,
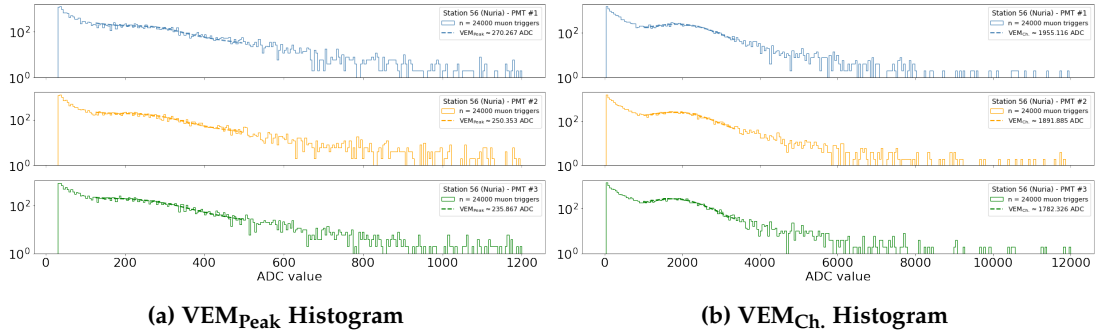
(a) VEM$_{\text{Peak}}$ Histogram

(b) VEM$_{\text{Ch.}}$ Histogram

Figure 2.4: (a) The maximum value of each muon trace is histogrammed in order to gain information about the current value of I_{Peak} of a station. **(b)** The conversion factor from recorded ADC values to Q_{Peak} is given from the histogrammed sum of each muon trace.

that is subsequently filled with low-energy events, which (in general) didn't satisfy any other trigger but still contain useful information [21].

By histogramming the maximum value (sum) of each trace, the plot shown in Figure 2.4a (Figure 2.4b) can be obtained. It becomes apparent that the number of events per bin largely follows a power law with negative spectral index. This is expected considering the discussion in chapter 1. Noteable are characteristic deviations from this powerlaw, as these contain information about I_{Peak} and Q_{Peak}:

- Low energy events from e.g. e^-, e^+ that deposit their entire energy in the tank give rise to a surplus of events at lower ADC values.

- A characteristic (muon) hump appears in the bins $20-70$. This surplus is caused by omni-directional muons impinging onto the detector. Since the energy deposited by such muons is roughly constant, the center of the muon hump serves as an estimate of I_{Peak} (Q_{Peak}).

- (Not depicted in Figure 2.6) In similar plots from related works (c.f. [21, 24]) a drastic increase in bin occupations towards the tail end of the histograms can be observed. This is attributed to an increased bin size from 1500 ADC counts onwards, which reduces the amount of data per station sent to CDAS. In the example plots referenced here, a constant binning is chosen instead. This difference is mentioned here to avoid possible confusion.

In this fashion, the average response of the WCD to a through-going muon can be estimated by e.g. fitting a gaussian distribution to the muon hump. However, there exists a systematic difference between the response to a vertical or an omni-directional muon. Consequently, correctional factors need to be applied to the analysis results. These have been determined in previous experiments [25]. Finally, one arrives at an estimate for the conversion factor between ADC counts and VEM$_{\text{Peak}}$, VEM$_{\text{Ch.}}$.

2.2.3 Online calibration

Baseline estimation

Each SD station has an autonomous estimate of its' three WCD PMT baselines. They are defined simply as the mean of all first bins for each trace contained in the respective muon buffers (see subsubsection 2.2.3). This baseline estimate is used to set the thresholds of the hardware triggers discussed in **??**.

Estimation of I_{Peak} and Q_{Peak}

Due to the limited computational resources in each station, the determination of I_{Peak} and Q_{Peak} at station-level is fairly naive. Nevertheless, the σ-δ-method shown here has proven to be incredibly robust over the lifetime of the SD array [11].

In the beginning, the to-be-estimated value $I_{\text{Peak}}^{\text{est.}}$ ($Q_{\text{Peak}}^{\text{est.}}$) is set to the same, predefined value for all PMTs. A simple single-bin calibration trigger requiring all available WCD PMTs to be above a threshold of $t_{70} = 1.75\, I_{\text{Peak}}^{\text{est.}}$ above baseline plus a given PMT exceeding $2.5\, I_{\text{Peak}}^{\text{est.}}$ is used to determine a calibration trigger rate. If for some reason not all three WCD PMTs are functional, the thresholds are altered according to Table 2.1. What follows is an iterative procedure to approximate I_{Peak} (Q_{Peak}):

1. Calculate the trigger rate $r_{\text{cal.}}$ of the calibration trigger over a time $t_{\text{cal.}} = 5\,\text{s}$.

2. Adjust $I_{\text{Peak}}^{\text{est.}}$ ($Q_{\text{Peak}}^{\text{est.}}$) by $\pm\delta$ if $\pm(r_{\text{cal.}} - 70\,\text{Hz}) \geq 2\,\text{Hz}$, with $\delta = 1\,\text{ADC}$ initially.

3. If $t_{\text{cal.}} < 60\,\text{s}$ increase $t_{\text{cal.}}$ by $5\,\text{s}$. If $\delta > 0.1\,\text{ADC}$ decrease δ by $0.1\,\text{ADC}$.

4. While $t_{\text{cal.}} < 60\,\text{s}$ jump to step 1, else return $I_{\text{Peak}}^{\text{est.}}$ ($Q_{\text{Peak}}^{\text{est.}}$).

Table 2.1

n_{PMT}	t_{70}
1	2.85
2	2.00
3	1.75

2.3 Event Reconstruction

If an event has been detected (subsection 2.3.1) it is reconstructed at CDAS level, where information from all relevant detectors is conglomerated. From the observed shower footprint in the SD array as well as the (if available) longitudinal profile measured by the FD stations follows an estimate on arrival direction (subsection 2.3.3), energy
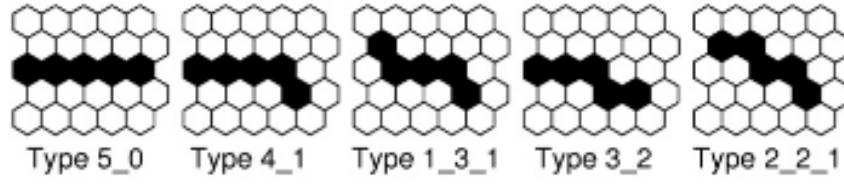
Figure 2.5: Fundamental shape of tracks considered straight. Image from [14].

(subsection 2.3.4) and primary particle (subsection 2.3.5). As the work presented in this thesis solely deals with the surface detector of the Auger observatory, this section focuses heavily on the SD reconstruction. Addendums towards FD reconstruction are given where needed.

2.3.1 Trigger procedure

The flux of cosmic rays espically at the highest energies is barely of the order of $1\,\mathrm{km}^{-2}\,\mathrm{yr}^{-1}$ [26]. Consequently, most signals observed by the Auger observatory stem from low-energy cosmic muons and not extensive air showers. This is reflected in the hierarchical structure of the triggers, which effectively reject such events. The overall event detection is split up into three tiers, T1, T2 and T3, where T3 implies the detection of an extensive air shower by either the FD or the SD (or both).

T1 trigger

T1 level triggers are implemented at the lowest possible level. This means each FD eye or each SD station raises T1 triggers autonomously. They serve as a first indicator on whether or not a signal of any kind is present. For the most part, this is realised by checking for elevated signal strengths, i.e. for hot pixels in a FD telescopes image or PMT outputs of an SD station that are significantly above baseline. The respective trigger thresholds are calibrated such that the nominal trigger rate during operation is roughly 100 Hz [14, 13].

T2 trigger

T2 level triggers occur at the same location as T1-type triggers. They are different in their more stringent conditions on the signal size or shape. This for example entails track shape identification for the FD telescopes, where straight tracks (see Figure 2.5) of hot pixels are identified. If the resulting pixel track passes an additional quality cut that rejects e.g. lightning signals, the T2 is directly promoted to a T3 trigger (= Event). For the SD, an exact discussion of T2 triggers is given in **??**. A single tank on average records T2-type events at a rate of 20 Hz and forwards this information to the CDAS along with a timestamp. There, incoming information of all tanks is scanned for spatial and temporal correlations, which indicate the presence of an extensive air shower.

T3 trigger

T3 type triggers, or event type triggers are (with the exception of FD events, which have been discussed above) built from distributions of at least three SD stations next to each other that recorded a T2 trigger in close temporal succession. Upon the detection of such a pattern a readout command is issued to all nearby stations. Their recorded FADC traces as well as calibration information are forwarded to CDAS if the station observed a T1/T2 event within an appropriate timespan of order $O(\mu s)$ before or after the T3 pattern occurence. Such a modus operandi enables an accurate reconstruction of the shower footprint by including stations that did not participate in the initial T3 trigger. This extends to FD issued T3 triggers, where potential information from SD stations in the vicinity of the FD-reconstructed shower core position is requested.

2.3.2 Core position

All reconstruction algorithms presented in the following subsections rely in one form or the other on an accurate determination of where the shower was recorded above the observatory. Hence the center of the shower footprint, the shower core, must be estimated at the beginning of the analysis chain.

Without any prior knowledge, a first guess as to where the shower core is located can be made by calculating the barycenter of all participating stations. In this fashion, a weighted mean of all station locations is constructed weights equal to the square root of the corresponding signal strength [13].

The presented approach fails if only parts of the shower are contained within the SD event. This occurs espically at the edges of the SD array, or in the vicinity of faulty WCDs. A fiducial trigger, $NT5$ is employed to mitigate this problem. $NT5$ requires at least N active stations around the SD detector that recorded the largest signal [27].

2.3.3 Arrival direction

The shower footprint measured by the SD (example given in Figure 2.6a) corresponds to the projection of the shower plane onto the detector plane, i.e. the ground. It can be assumed that the shower plane has a fixed (hyperbolic [28]) shape and propagates at the speed of light along the primary particles trajectory. With this knowledge, estimating the arrival direction becomes a task of minimizing the difference between measured and expected arrival times given by an example shower axis anchored at the reconstructed shower core. The axis for which the summed differences is minimal corresponds to the most likely arrival direction of the primary particle.

Naturally, the expected variance on the reconstructed ϕ and θ diminishes the more stations participate in the combined fit. The angular resolution thus decreases for larger energies of the primary particle. This can be seen in Figure 2.6b. In any case, the angular resolution even at smaller energies is better than 2.2°. For hybrid events,
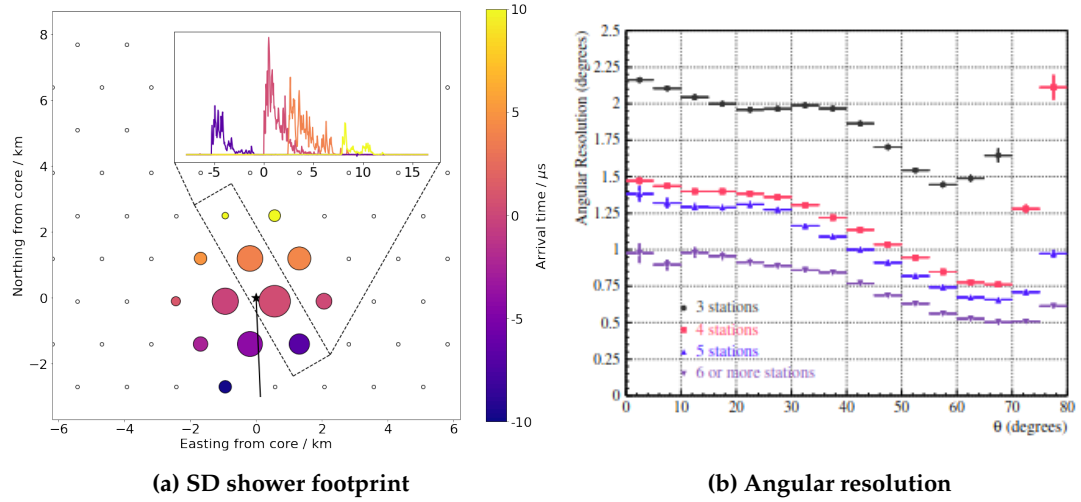
(a) SD shower footprint

(b) Angular resolution

Figure 2.6: (a) An example shower footprint recorded by the individual SD tanks (circles). The measured signal strength and arrival time is encoded in the size and color for each station. Tanks that haven't recorded any signal are shown colorless. For a subset of stations the respective VEM trace and consequently the propagation of the signal in the SD detector is shown in the inset plot on the top right. **(b)** The angular resolution as a function of θ for energies exceeding $3\,\mathrm{EeV}$. Image from [28].

where the shower has also been detected by the FD, the angular resolution is greatly increased to about $0.6°$ [28].

2.3.4 Energy estimation

2.3.5 Primary particle

Bibliography

[1] Robert A Millikan and G Harvey Cameron. "The origin of the cosmic rays". In: *Physical review* 32.4 (1928), p. 533.

[2] Thomas H Johnson. "A note on the nature of the primary cosmic radiation". In: *Physical Review* 54.5 (1938), p. 385.

[3] Nobel Media AB. *Press release.* `https://www.nobelprize.org/prizes/physics/1936/summary/`. Accessed: 18th Jul. 2022. 1936.

[4] Pierre Auger et al. "Extensive cosmic-ray showers". In: *Reviews of modern physics* 11.3-4 (1939), p. 288.

[5] Sergey Ostapchenko. "Status of QGSJET". In: *AIP Conference Proceedings.* Vol. 928. 1. American Institute of Physics. 2007, pp. 118–125.

[6] I Goldman et al. "Implications of the supernova SN1987A neutrino signals". In: *Physical review letters* 60.18 (1988), p. 1789.

[7] J Abraham et al. "Measurement of the energy spectrum of cosmic rays above 1018 eV using the Pierre Auger Observatory". In: *Physics Letters B* 685.4-5 (2010), pp. 239–246.

[8] Alexander Aab et al. "Searches for anisotropies in the arrival directions of the highest energy cosmic rays detected by the Pierre Auger Observatory". In: *The Astrophysical Journal* 804.1 (2015), p. 15.

[9] Hannes Alfvén. "Existence of electromagnetic-hydrodynamic waves". In: *Nature* 150.3805 (1942), pp. 405–406.

[10] Enrico Fermi. "On the origin of the cosmic radiation". In: *Physical review* 75.8 (1949), p. 1169.

[11] Alexander Aab et al. "The pierre auger observatory upgrade-preliminary design report". In: *arXiv preprint arXiv:1604.03637* (2016).

[12] The Pierre Auger Collaboration. *Timeline of the Pierre Auger Observatory.* `https://auger.org/observatory/timeline-observatory`. Accessed: 04th Oct. 2022. 2022.

[13] Alexander Aab et al. "Reconstruction of events recorded with the surface detector of the Pierre Auger Observatory". In: *Journal of Instrumentation* 15.10 (2020), P10021.

[14] Jorge Abraham et al. "The fluorescence detector of the Pierre Auger Observatory". In: *Nuclear Instruments and Methods in Physics Research Section A: Accelerators, Spectrometers, Detectors and Associated Equipment* 620.2-3 (2010), pp. 227–251.

[15]   Darko Veberič. *Auger array*. `https://web.ikp.kit.edu/darko/auger/auger-array/auger_array-pdf/auger_array-ad.pdf`. Accessed: 19th Jul. 2022. 2021.

[16]   The Pierre Auger Collaboration. *AugerPrime*. `https://auger.org/observatory/augerprime`. Accessed: 06th Nov. 2022.

[17]   João de Mello Neto, ed. *Physics and astrophysics of ultra-high energy cosmic rays: recent results from the Pierre Auger Observatory*. NUCLEUS - 2020.

[18]   Antonella Castellina. "AugerPrime: the Pierre Auger observatory upgrade". In: *EPJ Web of Conferences*. Vol. 210. EDP Sciences. 2019, p. 06002.

[19]   Jörg R Hörandel. "Precision measurements of cosmic rays up to the highest energies with a large radio array at the Pierre Auger Observatory". In: *EPJ Web of Conferences*. Vol. 210. EDP Sciences. 2019, p. 06005.

[20]   Valerio Verzi et al. "The energy scale of the Pierre Auger Observatory". In: *Proceedings of the 33rd ICRC, Rio de Janeiro, Brasil* (2013).

[21]   Xavier Bertou et al. "Local-Station Calibration - The Missing Manual". GAP 2022-0?? Oct. 2022.

[22]   Tobias Schulz et al. "New Baseline Algorithm for UB Traces". GAP 2022-045. Sept. 2022.

[23]   Tobias Schulz et al. "New Baseline Algorithm for UUB Traces". GAP 2022-0?? Dec. 2022.

[24]   Alexander Streich et al. "Performance of the upgraded surface detector stations of the Pierre Auger Observatory". In: *Verhandlungen der Deutschen Physikalischen Gesellschaft* (2018).

[25]   P.S. Allison et al. "Surface Detector calibration in the Engineering Array". GAP 2002-028. July 2002.

[26]   Anthony M Hillas. "The origin of ultra-high-energy cosmic rays". In: *Annual review of astronomy and astrophysics* 22 (1984), pp. 425–444.

[27]   J Abraham et al. "Trigger and aperture of the surface detector array of the Pierre Auger Observatory". In: *Nuclear Instruments and Methods in Physics Research Section A: Accelerators, Spectrometers, Detectors and Associated Equipment* 613.1 (2010), pp. 29–39.

[28]   C Bonifazi. "Angular resolution of the pierre auger observatory". In: *29th International Cosmic Ray Conference (ICRC29), Volume 7*. Vol. 7. 2005, p. 17.